# Molecular Beams in Space: Sources of OH(A→X) Emission in the Space Shuttle Environment†

**Lawrence S. Bernstein**

*Spectral Sciences Inc., 99 South Bedford Street, # 7, Burlington, Massachusetts 01803*

**Yu-hui Chiu**

*Institute for Scientific Research, Boston College, Newton, Massachusetts 02159*

**James A. Gardner and A. Lyle Broadfoot**

*Lunar and Planetary Laboratory, University of Arizona, Tucson, Arizona 85721*

**Marsha I. Lester and Maria Tsiouris**

*Department of Chemistry, University of Pennsylvania, Philadelphia, Pennsylvania 19104*

**Rainer A. Dressler and Edmond Murad***

*Space Vehicles Directorate, Air Force Research Laboratory, Hanscom AFB, Massachusetts 01731*

*Received: April 28, 2003; In Final Form: August 26, 2003*

OH(A→X) emission bands have been observed in the molecular beam jets produced by Space Shuttle engine exhaust using the GLO imager spectrograph located in the payload bay. Spectra were collected at a resolution of 4 Å for both daytime and nighttime solar illumination conditions, all at an altitude of ∼390 km. A spectral analysis is presented that identifies and quantifies four separate OH(A) excitation processes. These include (i) solar-induced fluorescence of the OH(X) in the exhaust flow, (ii) solar-induced photodissociation of $H_2O$ in the exhaust at the strong Lyman-α solar emission line (1216 Å), (iii) solar-induced photodissociation of $H_2O$ in the far UV, at shorter wavelengths than Lyman-α, and (iv) luminescent collisions between atmospheric species and exhaust constituents, most probably the reaction $O + H_2O \rightarrow OH(A) + OH(X)$. Process (i) produces a very rotationally cold and spectrally narrow component due to the rapid cooling of the OH(X) in the supersonic expansion of the exhaust flow. Processes (ii) and (iii) produce extremely excited OH(A), not well characterized by thermal vibrational or rotational distributions. The $O + H_2O$ chemiluminescent reaction has a substantial activation energy, 4.79 eV, and is only slightly above threshold for the ram geometry, where the engine exhaust is directed into the atmospheric wind. Evidence for process (iv) is observed in the night ram but not the night perpendicular exhaust atmospheric interaction, consistent with the threshold energy. Through the use of a nonequilibrium spectral emission model for OH, the integrated intensity, spectral distribution, and OH(A) internal state characterization for each of the above processes was deduced. Additional confirmation of the analysis is provided through the use of a model simulation of the space experiment to predict the total integrated intensities for processes (i) and (ii), for which the underlying spectroscopy, absorption cross sections, and solar excitation intensities are well established. Analysis of process (iii) has established, for the first time, a value for the far-UV conversion efficiency of absorbed photons to OH(A) photons of 0.26, which is twice the established value for Lyman-α. Under the assumption that $O + H_2O$ collisions are the source of process (iv), the analysis has established a chemiluminescence cross section at ram conditions of $1.7 \times 10^{-2}$ Å$^2$. Evidence of OH(A) emission bands from predissociated vibrational levels suggests that the total reaction cross section for process (iv) may be significantly higher. While this cross section assumes a single-step reaction of O with $H_2O$, the possibility of a two-step process of O with other plume species has yet to be explored.

## I. Introduction

Over the years, significant advances have been made in laboratory experimental techniques to study the gas-phase dynamics of chemical reaction systems in ever-increasing detail. However, there remain systems that are difficult to capture in a laboratory because experimental approaches either lack the necessary sensitivity due to low number densities and small observation volumes, or do not provide the necessary control of reactant energies and densities. Remote passive optical observations of natural and man-made space-based environments have the advantage of overcoming the shortage of emitting species in a laboratory. In instances where the coupled chemical

† Part of the special issue "Charles S. Parmenter Festschrift".

10.1021/jp035143x CCC: $25.00 
Published on Web 10/21/2003

processes are well characterized, they can provide a more direct and sensitive measure of a chemical rate coefficient. For example, a number of rate coefficients of radical−radical reactions have initially been determined from observations of astrophysical environments in conjunction with laboratory studies; a specific example of such a reaction is the radiative association reaction $C^+ + H_2 \rightarrow CH_2^+ + h\nu$. This reaction was postulated[1] to provide a formation mechanism for the observation of CH in the interstellar medium. A rate coefficient of $3 \times 10^{-16}$ cm$^3$ s$^{-1}$ was first derived from the observation and from a postulated chemical mechanism. Later calculation of this rate coefficient[2] derived a value of $10^{(-16\pm1.5)}$ cm$^3$ s$^{-1}$. More recent laboratory measurements[3] have shown the rate coefficient to be $(7.0 \pm 3.5) \times 10^{-16}$ cm$^3$ s$^{-1}$.

As demonstrated recently,[4,5] molecular beams emitted from a low Earth orbit (LEO) spacecraft engine, such as a Space Shuttle Primary Reaction Control System (PRCS) engine, offer an attractive means to observe luminescent processes that follow from the hyperthermal interaction between the beam species and the ambient atmosphere. At typical LEO altitudes (200−400 km), the thermosphere consists of ∼70% atomic oxygen and ∼25% $N_2$. Because the spacecraft orbit velocity is approximately 7.8 km s$^{-1}$, an oxygen atom penetrates the spacecraft environment with a "laboratory energy" approaching 5 eV, depending on the orbit inclination and the atmospheric corotational speed. This results in an average center-of-mass collision energy exceeding 2.3 eV for collisions with $H_2O$, a primary species of a contaminant cloud that engulfs the orbiter. Water is also a major species in the exhaust emanating from the spacecraft maneuvering engines. The flow from these engines has the characteristics of a supersonic jet with free-flow velocities exceeding $3 \times 10^3$ m s$^{-1}$, thereby adding additional kinetic energy to collisions with atmospheric constituents. Consequently, experiments conducted from a LEO platform can be exploited to investigate the dynamics at hyperthermal translational energies that are difficult to create in a laboratory. Knowledge of the precise orbital conditions and optical interference sources then permits the extraction of rate coefficients for luminescence processes. It is worth mentioning here that contamination, especially $H_2O$ from outgassing and from thruster exhaust, affects all space or space-bound vehicles, as has been shown for rockets,[6,7] for the Space Shuttle[6,8,9] and has been demonstrated in laboratory simulations.[10]

During the 1990s, a suite of imagers and spectrographs called GLO was successfully flown on five different missions in the Space Shuttle bay providing a wealth of optical data of the Space Shuttle and near-Earth optical environment covering an unprecedented spectral range, 1150−9000 Å, at resolutions ranging from ∼4 (UV) to ∼10 Å (IR).[11,12] One of the more puzzling observations of the GLO experiments,[13] and of parallel, lower resolution measurements taken from the space station Mir,[14,15] was a prominent band centered at 3086 Å that was observed in darkness during spacecraft maneuvers where the engine was fired directly into the atmospheric wind. From the high-resolution GLO measurements it was concluded that the UV band was due to OH $A^2\Sigma^+ - X^2\Pi$ fluorescence. The radiation was most prominent at many tens of meters from the engine nozzle, where it can be safely assumed that the exhaust jet has reached terminal and very cold translational and rotational temperatures in the supersonic expansion and is subject to free-stream conditions. The fact that the emissions were more prominent at distances beyond 10 m than immediately after the nozzle led to the conclusion that the band arises from luminescence produced by atmosphere−exhaust collisional interactions.[13]

Attempts have been made to reconcile the observations through direct simulation Monte Carlo (DSMC) calculations of the orbital environment assuming the reaction[14−18]

$$O(^3P) + H_2O \rightarrow OH(A^2\Sigma^+) + OH(X^2\Pi) - 4.79 \text{ eV} \quad (1)$$

Note that the reaction threshold exceeds the chemical energy available from the kinetic energy of the oxygen atoms alone. This channel is opened only when the exhaust jet of the engine is directed into the atmospheric wind, where the exhaust $H_2O$ velocity provides additional translational energy to the collision system. The rate coefficient for this chemiluminescent process has not been measured, nor has it been calculated. Previously, modelers estimated a rate coefficient from the Arrhenius form of the temperature-dependent rate coefficient reported for the reaction leading to ground state hydroxyl molecules,[19,20] adjusted for the activation energy as well as for the fact that only one OH product is electronically excited:

$$k_1 = 3.8 \times 10^{-15} T^{1.3} \exp(-E_a/kT); \qquad E_a = 4.79 \text{ eV} \quad (2)$$

This estimate has been reported to lead to a substantial overprediction of the absolute OH(A−X) radiance.[16,21] Erofeev et al.[22] provided an estimated upper limit of $10^{-2}$ Å$^2$ for the emission cross section based on the analysis of radiance observed when a Soyuz engine was fired into the atmospheric wind. This is approximately 2 orders of magnitude less than the rate law applied in the models.

Orient et al.[23] conducted crossed-beam measurements of O + $H_2O$ collisions using a sophisticated fast-atomic oxygen beam and observed unresolved UV emissions in the 3000−4000 Å range. Although the onset seemed to be near the threshold energy for OH(A) formation, the signal-to-noise level was poor, so that definitive conclusions could not be made about the efficiency of reaction 1, nor could an estimate of the absolute cross section be made. More recently, Matsika and Yarkony[24] reported calculations of the potential energy surfaces associated with reaction 1. Two conical intersection seams were identified through which the ground state reactants can access the electronically excited product surfaces. The lowest energy points of the seams are at collinear geometries, which represent an important constraint on the initially bent system. This suggests that reaction 1 is possible but inefficient near threshold, and other processes could compete in producing the observed radiance.

Other important sources of OH(A) in the spacecraft environment (high-density flame reactions excluded) are the photo-induced processes:

$$H_2O + h\nu \rightarrow OH(A) + H \quad (3)$$

$$OH + h\nu \rightarrow OH(A) \quad (4)$$

These processes can be expected to be prominent in day-lit conditions. Process 3, however, must also be considered in the night sky, where there is still significant VUV radiation from resonant atomic scattering from Earth's geocorona, especially when the sun is not far below the horizon. A primary contributor of process 3 is H Lyman-α radiation at 1216 Å that provides sufficient energy to produce OH(A) with significant rotational and vibrational excitation.[25−27] There is a substantial concentration of OH(X) present in the exhaust of space engines due to

the high temperatures and *kinetically controlled* conditions within the engines.[28−30] Depending on the type of engine, the mole fraction may reach values as high as $4 \times 10^{-3}$. In contrast, *equilibrium* estimates of the exhaust OH(X) mole fraction are insignificant, $<10^{-6}$. Direct solar excitation of OH in the engine exhaust (reaction 4) is expected to produce rotationally cold OH(A) emission. A high-resolution spectrograph should thus be capable of differentiating between the photoinduced processes 3 and 4.

A key hindrance to a persuasive interpretation of the observed OH(A) radiance has been the lack of quantitative, high-resolution, fully reduced spectra taken at different, well-characterized space environmental conditions. Unlike laboratory experiments, remote sensing conditions are rarely fully reproducible, and a proper analysis depends on knowledge of many geomagnetic and measurement geometry parameters. The validation of a chemical model depends on the comparison of a significant number of measurements at known conditions. The present work is the result of a concerted effort at reducing and closely examining a vast set of spectral data stemming from the GLO missions with particular emphasis on the OH(A−X) band emissions. A small subset of these data is analyzed and presented in this paper. For the first time, daytime and night-sky spectra are compared, providing additional information on sources of OH(A). We also compare night-sky spectra where the exhaust is directed both into the atmospheric wind (ram) and perpendicular to the velocity vector of the orbiter, thus providing a direct comparison between radiances at different exhaust−atmosphere interaction energies. In the following section, the orbital conditions of the respective GLO mission, GLO-2 on Space Shuttle mission STS-63, the GLO instrument, the spectral data reduction procedure, and the chemical constituents of the Shuttle engine exhaust will be briefly described. In section III, we present a representative survey of spectral measurements at different conditions, the spectral analysis of a subset of measurements, and the quantification of photoinduced processes using a one-dimensional model that takes optical opacity into account. In section IV, we discuss the results in the context of reaction 1 and derive an emission cross section that we compare with predictions from the previous estimate of eq 2.

## II. Experimental Section

**A. Space Experimental Conditions.** The data presented in this work were acquired from GLO-2 aboard the STS-63 Space Shuttle mission that occurred on February 5−11, 1995. The orbital inclination angle was 51.6° to accommodate a rendezvous with the space station Mir. Figure 1 provides a schematic of the STS-63 orbit. At the ∼390 km operational altitude, the oxygen atom densities ranged between a nighttime minimum of $\sim 2 \times 10^7$ and a daytime maximum of $\sim 8 \times 10^7$ cm$^{-3}$. The thermospheric temperature for the present mission varied significantly with respect to latitude and local time from ∼700 to 960 K. The thermospheric parameters associated with a particular measurement were retrieved from the MSIS thermosphere model.[31−33] The orbital velocity at 390 km is $7.67 \times 10^3$ m s$^{-1}$. Assuming corotation of the thermosphere, the spacecraft velocity with respect to the atmosphere ranges between 7.37 and $7.38 \times 10^3$ m s$^{-1}$ in the present west−east orbit, dependent on the orbiter latitude. It is worth mentioning that observations suggest that dynamic interaction between the ionosphere and the thermosphere induces thermospheric super-rotation, leading to a 6−8% faster rotation than the Earth.[34]

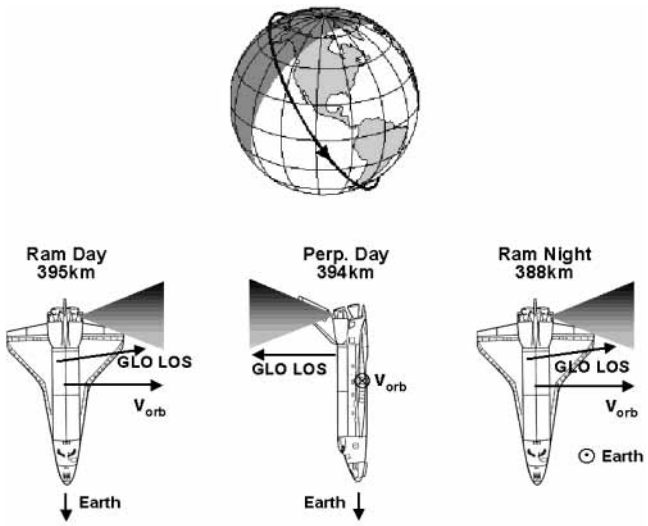


**Figure 1.** Overview of the orbital and measurement geometry for the analyzed GLO data obtained during the STS-63 mission.

**TABLE 1: Mole Fractions, $\chi$, of Chemical Constituents Calculated for the Exhaust of a PRCS Shuttle Engine**[a]

| species | $\chi$ | species | $\chi$ |
|---|---|---|---|
| $N_2$ | 0.33 | $H_2$ | 0.042 |
| $H_2O$ | 0.41 | OH | 0.0044 |
| CO | 0.07 | NO | 0.013 |
| $CO_2$ | 0.09 | H | 0.027 |

[a] The calculations are based on work by Viereck et al.[30]

The primary source of water contamination on the Space Shuttle is from engine exhaust; a secondary source, the outgassing of surfaces, is particularly important in the early phase of the flight.[29,35] After a day or two, outgassing becomes less important and the pressure in the environment of the Space Shuttle becomes comparable to the ambient pressure. In this paper we analyze the optical signals generated by the most intense and the most persistent of these sources, namely the exhaust of engines. The data pertain to the 870 lb thrust PRCS engines that use $N_2O_4$−monomethylhydrazine (MMH) fuel. The products of the exhaust based on nonequilibrium calculations are shown in Table 1.[30] It is estimated that a PRCS firing lasting 0.72 s releases $5.5 \times 10^{25}$ neutral molecules or atoms.[28] For the experiments reported here, typical firings lasted ∼3 s, leading to a total number of neutrals ejected of $\sim 2 \times 10^{26}$. The implication of the composition data is that there is sufficient OH for direct excitation of, and $H_2O$ for chemical reaction with oncoming ambient O atoms, respectively.

A large number of exhaust-induced optical spectra have been examined for different PRCS engines and firing geometries. Figure 1 provides an overview of the engine firings and the GLO instrument position and line-of-sight (LOS) which produced the spectra presented in section III. We present both nighttime and daytime measurements at exhaust−atmosphere interaction angles of attack of 180° (ram) and 90° (perpendicular). A significant number of spectra at perpendicular night conditions were examined. Except at twilight conditions, no OH(A−X) emissions could be identified. Table 2 provides the important parameters of the engine firings associated with the spectral recordings presented in this work. While the local time difference between the daytime measurements is significant, in actuality, they were recorded only 6 min apart in universal time (UT). The orbit leg defines whether the velocity vector at the time was in a north−south (descending) or south−north

**TABLE 2: Summary of Important Parameters Associated with the Three PRCS Engine Firings Depicted in Figure 1[a]**

| firing | local time | altitude (km) | lat. (deg) | long. (deg) | leg | $v_{rel}$ ($10^3$ m s$^{-1}$) | $T$ (K) | [O] ($10^7$ cm$^{-3}$) |
|---|---|---|---|---|---|---|---|---|
| ram day | 9:26 | 397.2 | −31 | 283 | descending | 10.87 | 801 | 4.50 |
| perpendicular day | 11:32 | 403.5 | −45 | 305 | descending | 8.156 | 837 | 5.41 |
| ram night | 19:27 | 388.0 | 8.5 | 142.5 | ascending | 10.88 | 767 | 3.04 |

[a] Lat. and long. refer to the shuttle latitude and longitude position; leg defines whether the shuttle was traveling in a south−north (ascending) or north−south (descending) direction. $v_{rel}$ is the nominal relative velocity between O atoms and exhaust molecules assuming an exhaust velocity of $3.5 \times 10^3$ m s$^{-1}$.[28,30] $T$ and [O] are the thermospheric temperature and oxygen atom density, respectively, as determined with the MSIS thermospheric model.[31−33,62] All engine firings occurred on February 10, 1995.

(ascending) direction. $v_{rel}$ is the relative velocity given by

$$v_{rel} = |\mathbf{v}_{rel}| \qquad (5)$$

$$\mathbf{v}_{rel} = \mathbf{v}_{orb} - \mathbf{v}_{cor} + \mathbf{v}_{ex}$$

where $\mathbf{v}_{orb}$ is the orbiter velocity vector, $\mathbf{v}_{cor}$ is the atmospheric corotation vector, and $\mathbf{v}_{ex}$ is the exhaust velocity vector. An axial exhaust velocity of $3.5 \times 10^3$ m s$^{-1}$ was assumed, which originates from the exit velocity of $3 \times 10^3$ m s$^{-1}$ plus an additional $0.5 \times 10^3$ m s$^{-1}$ attained in the vacuum expansion.[28,30]

The ram measurements involved the L2L engine, while the perpendicular measurement observed a firing from the L2U engine. The instrumental pointing directions are shown in Figure 1. For the ram day measurement, the azimuthal angle of the spectrograph was −95°, as referenced with respect to the orbiter main axis. The elevation angle was 5° with respect to the image plane of Figure 1. At this viewing geometry, the line-of-sight intersects the thrust axis at a distance of >50 m from the nozzle exit, thereby avoiding emissions from the hot nozzle area of the exhaust while observing substantial column densities of the exhaust−atmosphere interaction region. In the perpendicular day measurement, the elevation angle was 90°, resulting in a LOS parallel to and displaced by ∼5 m from the thrust axis.

**B. The GLO Instrument.** The space-borne GLO instrument has been described in detail before and was placed in the rear section of the shuttle bay during the STS-63 mission (see Figure 1).[5] It comprises a nine-section spectrograph, three monochromatic imagers, and a TV camera, all boresighted to view in the same direction. The spectrograph and imagers have intensified-CCD (ICCD) focal-plane detectors. The nine slightly overlapping spectrograph sections permit simultaneous recording of the spectrum from 115.0 to 900.0 nm with a spectral resolution of about 4−10 Å. Their combined focal-plane image is 4500 pixels wide in the wavelength (dispersion) dimension, perpendicular to the slit, and 192 pixels in the spatial dimension, along the slit. The slit image at the detector is a narrow portion of the image of the distant object being observed, preserving spatial resolution in the slit-length direction. The design of slit and foreoptics affords a field of view of 0.2 × 8.5°. The spectrograph was designed to record simultaneously as much information as possible from a single column of gas, with a spectral resolution good enough to determine the intensity and the rovibrational structure of molecular emissions.

The instrument head is mounted on a scan platform that can rotate the field of view in two orthogonal directions (azimuth and elevation), thereby permitting viewing in almost any direction. The TV-camera image is used while in flight to select the view direction, track the day or night Earth limb, and hold stars steady in the spectrograph slit for spectral calibrations and occultation experiments. A computer is dedicated to carrying out preprogrammed, complex experiment sequences that are time tagged and/or ground commanded. The instrument is therefore autonomous and capable of continuous operation throughout a 14-day mission. Science and engineering data are returned on communications links via the TDRS satellites at a total data-return rate of 1.5 Mbits/s. A rewriteable 512-MB optical disk records during loss of signal on the TDRS link. Data acquisition and downloading are described in separate publications.[13,36]

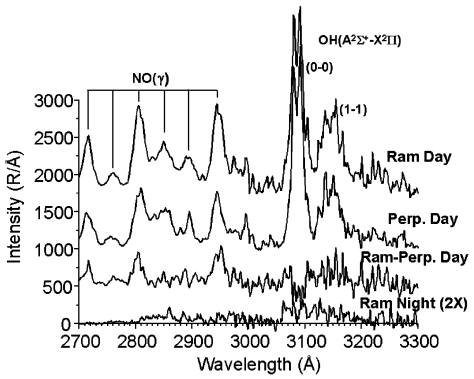


**Figure 2.** GLO spectral data corresponding to measurement geometries depicted in Figure 1. The spectra have been vertically displaced for presentation purposes.

**C. Spectral Data Reduction.** The GLO data are processed and analyzed using two utility programs, SIBYL and GLOview, provided by the Lunar and Planetary Laboratory of the University of Arizona.[11] SIBYL handles the data returned from ICCD spectrographs and imagers, while GLOview visualizes the geometric viewing parameters such as the spacecraft position with respect to Earth, the sun, and the stellar background, the GLO instrument pointing direction, and the orientation of the spectrograph slit and imagers. Using the SIBYL program, a typical spectrum is obtained by the following procedures: An optical background hyperspectral image is obtained by identifying an image frame recorded shortly prior to the engine firing at the same pointing geometry. The exposures are then normalized with respect to time (1 s), and bad pixel data are removed. A mission and spectrograph section dependent transformation is then applied to the pixel array in order to properly align the slit dimension with respect to the vertical axis of the array. The background data are then subtracted from the exhaust recording, and a spectrum is obtained by generating a sum of pixel rows that cover the slit range of interest. The spectra are then calibrated with respect to wavelength and the intensity is converted to an absolute scale (R Å$^{-1}$, 1 R = 1 rayleigh = $10^6$ photons cm$^{-2}$ s$^{-1}$ integrated over all angles) with the use of ICCD spectral sensitivity curves.

## III. Results

**A. Space-Based Spectral Measurements.** Spectra in the 2700−3300 Å spectral range are presented for ram and perpendicular day and ram night conditions in Figure 2. They were originally recorded from a 2 s exposure at a resolution of 4 Å. The figure also includes a difference spectrum between the two daytime spectra. Except for the ram night spectrum, which is expanded by a factor of 2, all of the spectra are plotted

on the same vertical intensity scale. Structure due to the OH(A−X) 0−0 and 1−1 bands near 3080 Å (termed $\Delta v = 0$ bands) is apparent in all of the spectra. NO($\gamma$) band emissions can also be identified and are attributed to solar-induced fluorescence of NO in the exhaust. A substantial NO($\gamma$) signal is expected, since the NO exhaust mole fraction is larger than that for OH and the integrated absorption strength of NO($\gamma$) is much larger than that for OH(A). Because the NO($\gamma$) absorption is quite optically opaque, the observed fluorescence will be quite sensitive to the geometric position of the detector, exhaust flow, and the sun, as reflected by the significant differences in the ram and perpendicular day observations. The NO($\gamma$) bands will not be further discussed in this work, except that they interfere with the OH(A) $\Delta v = -1$ bands at ∼2800 Å. The similarity between the ram and perpendicular OH(A−X) spectra in daytime, with respect to both structure and intensity, suggests that these emissions are primarily attributable to photoexcitation processes.

The signal for the ram night spectrum is substantially weaker than the day spectrum, further confirming that photoexcitation plays a major role in the daytime observations. No OH(A−X) emissions can be identified in perpendicular night measurements (not shown in Figure 2). The difference spectrum of the day measurements also reveals a broad band that, upon closer inspection, has features similar to the ram night spectrum. The comparison is somewhat obstructed at ∼3090 Å due to the higher intensity of the most intense OH(A−X) feature in the perpendicular measurement. This is attributed to optical opacity effects discussed in greater detail in section III.C. Nevertheless, the similarity between the difference day spectrum and the ram night spectrum suggests that the broad band at 3100 Å is due to a chemiluminescent process attributable to exhaust−atmosphere interaction, and that this process has a cross section that is significantly larger in the ram than in perpendicular conditions. This is also consistent with the fact that the nighttime OH(A−X) feature is weaker than the daytime difference spectrum, and relates to the lower nighttime atmospheric atomic oxygen density, as seen in Table 2. In the following, a quantitative analysis of the spectra is conducted based on these tentative conclusions.

**B. Spectral Analysis.** The intense OH(A−X) band observed at a perpendicular angle of attack in the day measurements appears to be dominated by photoinduced processes. As mentioned in the Introduction, two photoinduced processes 3 and 4 could contribute to such emissions. These two processes produce entirely different OH(A) vibrational and rotational populations. Direct excitation of exhaust OH with ∼3100 Å light produces a Franck−Condon vibrational distribution and a rotational temperature governed by the expansion-cooled OH(X) in the exhaust. Ly-α photodissociation of $H_2O$ at 1216 Å has been shown to yield a substantially hotter vibrational and rotational distribution of OH(A).[26,27] Photodissociation of $H_2O$ with far-UV radiation can be expected to result in an even hotter vibrational and rotational distribution, although laboratory measurements of the OH(A) product state distribution have not been carried out at these extreme wavelengths.

Figure 3 compares the perpendicular daytime spectrum to a spectrum calculated to provide a best fit of the OH(A−X) $\Delta v = 0$ features, assuming photoinduced processes (3) and (4) are in effect. The calculated spectrum was generated using a previously developed nonequilibrium radiative transfer code.[37] The code computes the emission−absorption spectrum for an optically opaque inhomogeneous column of thermally and nonthermally excited diatomic molecules. The populations of the upper and lower electronic states are specified, typically in terms of separate effective vibrational and rotational temperatures, for each computational segment of the emitting−absorbing path. Each emission−absorption line is explicitly considered using a precomputed spectral database consisting of line position, integrated strength, pressure broadening coefficient, and the vibrational and rotational energies of the upper and lower electronic states. While this code, which has a line position accuracy of ∼1 $cm^{-1}$, is adequate for the analysis reported here, we note the more recent development of similar nonequilibrium OH(A) emission models with somewhat improved spectral accuracy and intensity distributions.[38,39]

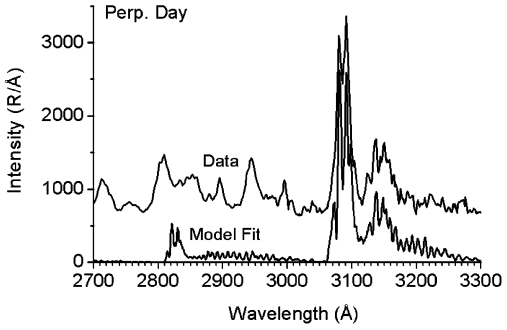


**Figure 3.** Comparison of the model fit to the perpendicular day GLO data. The data curve has been vertically displaced by +500 R/Å.

For application to the OH analysis, however, a few modifications were made to the code. The vibrational populations of the OH(A) state were specified individually, and a total vibration−rotation energy cutoff in the OH(A) state was introduced. In addition, a rotational state dependent weighting factor, $W = K^n$, where $K$ is the rotational quantum number, was applied to the rotational populations to approximately account for the highly non-Boltzmann rotational distributions found for OH(A) formed via ultraviolet induced dissociation of $H_2O$.[26,27] A value of $n = 1$ was empirically found to give a reasonable fit to the observed laboratory spectrum[27] for this OH(A) formation process. The simulations were limited to $v' \leq 4$ and $v'' \leq 3$.

The spectral parameters providing the best fit are given in Table 3. The individual components of the spectrum are shown in Figure 4. From the fits it can be deduced that the most intense feature is predominantly from solar resonance fluorescence, which also contributes nearly half of the total integrated OH(A−X) radiance. A rotational temperature of 150 K provides the best agreement between the calculated and observed spectra. The goodness of the fit, however, is substantially improved by adding a hot component produced in $H_2O$ photodissociation processes. The integrated intensity attributable to hot OH must be consistent with known far-UV radiance and the associated photoinduced conversion efficiencies. The latter is only known for Ly-α + $H_2O$[26] and results in insufficient intensity to fully reproduce the spectrum. The residual hot OH(A) signal can be accounted for assuming additional photoinduced processes from solar lines at shorter wavelengths, referred to as far-UV lines.

The $H_2O$ photodissociation contribution involves high rotational excitation of OH(A) that is not well represented by a thermal distribution. We have been able to satisfactorily reproduce the Ly-α laboratory results of Carrington[26,27] by applying a rotational temperature with an additional statistical factor given by the rotational quantum number, $K$. The distributions are truncated (Table 3) so that no contributions are allowed from energetically closed product channels. The OH(A) vibrational populations from Ly-α photodissociation of $H_2O$ were

**TABLE 3: Parameters Providing the Best Reproduction of the OH(A−X) Perpendicular Day Spectrum and the Ram Night Spectrum[a]**

| component | $P_{v'}$ ($v' = 0, 1, 2, 3, 4$) | $T_r'$ (K) | $W_K$ | $E_{max}$ (cm$^{-1}$) | integrated radiances (kR) |
|---|---|---|---|---|---|
| | | Perpendicular Day | | | |
| exhaust OH | $T_v' = 5\,000$[b] | 150 | 1 | 12 000 | 57 |
| Ly-α + $H_2O$ | 1.0, 0.85, 0.31, 0.04[c] | 40 000 | *K* | 8 500 | 27 |
| far UV + $H_2O$ | 1.0, 1.0, 1.0, 1.0, 1.0 | 40 000 | *K* | 12 000 | 40 |
| | | Ram Night | | | |
| reaction OH | 1.0, 1.1, 0.46, 0.86, 0.54 | 4 000 | 1 | 12 000 | 21 |

[a] $T_v'$ and $T_r'$ are the A state vibrational and rotational temperatures, $W_K$ is the additional weighting applied to account for nonthermal rotational distributions, and $E_{max}$ is the cutoff energy applied to account for either predissociation limits (12 000 cm$^{-1}$) or energy conservation. [b] A vibrational temperature was used to define the populations of the $v' = 0$ and 1 levels, and $P_{v'} = 0$ for $v' > 1$. [c] Populations from laboratory experiments.[26]

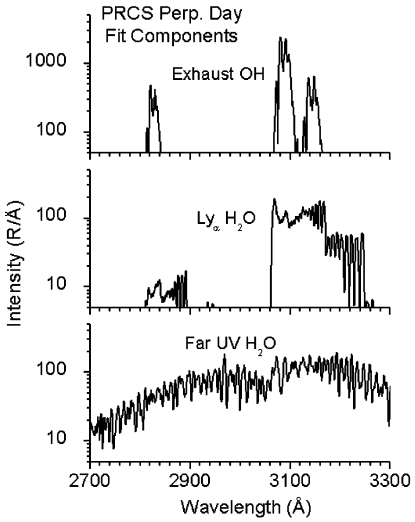


**Figure 4.** Spectral components for the model fit in Figure 3 corresponding to the photoinduced OH(A) emission processes. Note the 10-fold expanded vertical scale for the Ly-α and far-UV components.

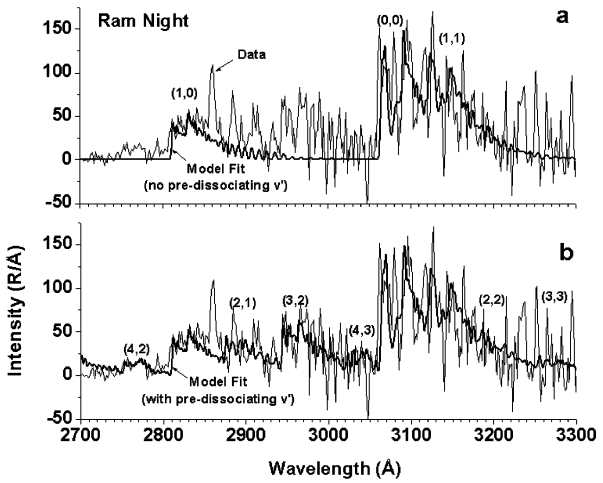


**Figure 5.** Comparison of the model fit to the night ram GLO data. The calculated spectra have been slightly spectrally degraded for improved comparison. (a) Calculated spectrum includes predissociation: i.e., predissociated states make an insignificant contribution. (b) Calculated spectrum neglects predissociation: i.e., all levels are assumed to radiate.

obtained from laboratory experimental results.[26] The far-UV component has not been previously measured in the laboratory. It was assumed that the Ly-α rotational distribution would apply and that the vibrational distribution would be considerably hotter due to the availability of >2 eV additional excitation energy. We have assumed an equal population of vibrational states for the OH(A) products.

Figure 5 compares the observed ram night OH(A−X) spectrum with modeled spectra. The model spectra have been degraded to slightly lower spectral resolution than the data to facilitate the comparison. They were generated with a maximum OH(A) internal energy cutoff of $E_{max} = 1.5$ eV. This corresponds to a reasonable upper limit to the amount of internal excitation available to the reactively produced OH(A) for the ram burn, taking into account the spread in atmospheric O atom velocities. The two model spectra correspond to different assumed limits with respect to the effect of predissociation on the OH(A) emission spectrum.[39−41] OH(A) levels with term energies exceeding 12 000 cm$^{-1}$ predissociate with rates significantly higher than the fluorescence rates.

In Figure 5a, only the nonpredissociating $v' = 0$ and 1 levels were included in the fit along with a rotational temperature of $T_r = 4000$ K. The comparison between the calculated spectrum and the ram night spectrum, however, indicates significant intensity between 2950 and 3000 Å that is not reproduced by the modeled spectrum. It appears that slightly too much baseline subtraction was applied to the experimental data in the spectrograph segment above 3000 Å. We estimate that the addition of a constant ∼ +25 R/Å to the data in this spectrograph segment would noticeably improve the model−data comparison.

In Figure 5b, the ram night spectrum is compared with a modeled spectrum that does not include predissociation and, therefore, includes emissions from $v' = 2$, 3, and 4 with steady state populations shown in Table 3. It is seen that the calculated (3,2) band reproduces the 2950−3000 Å band remarkably well. The model spectrum also accounts for a weaker feature at 2760 Å where the (4,2) band would be expected.[39,42] It is worth noting that similar bands have been observed in atmospheric pressure air plasmas.[38] There are a few features, such as the sharp bands at 2860, 2890, and 3235 Å, that are not accounted for by the calculated spectra for which no source can be identified.

**C. Integrated Radiance Analysis.** The observed integrated intensities from the solar-induced processes (Table 3) can be understood with reference to a simple model of the space experiment. The local number density, $\rho$, of the exhaust gases is given by the well-established Brook exhaust flow model,[43]

$$\rho = \frac{A \exp(-B(1 - \cos\theta))}{R^2} \tag{6}$$

where $A$ and $B$ are motor-specific constants, $R$ is the radial distance measured from the "point-source" motor, and $\theta$ is the angle measured from the thrust axis. The representation of the flow as a point source is valid for distances beyond ∼10 nozzle exit diameters. It applies to this analysis since the exit diameter of the Shuttle PRCS motor is 24 cm and the GLO instrument LOS typically intersects the exhaust flow beyond 5 m from the exit. For the PRCS motor, $A = 9.94 \times 10^{22}$ molecules cm$^{-1}$ and $B = 8.58$.

**TABLE 4: Spectral Parameters Used in the Model Intensity Predictions for the Solar-Induced Fluorescence of the Exhaust OH[a]**

| band ($v',v''$) | $\lambda_o$ (Å) | $F_\lambda$ (photons $s^{-1}$ $cm^{-2}$ $Å^{-1}$) | $G$ (photons $s^{-1}$ $mol^{-1}$) | $A$ ($s^{-1}$) | R | $\sigma^b$ ($cm^2$) |
|---|---|---|---|---|---|---|
| (0,0) | 3086 | $1.2 \times 10^{13}$ | $9.7 \times 10^{-4}$ | $1.5 \times 10^{6}$ | 1.0 | $6.0 \times 10^{-15}$ |
| (1,0) | 2826 | $6.0 \times 10^{12}$ | $1.0 \times 10^{-4}$ | $0.44 \times 10^{6}$ | 0.34 | $1.5 \times 10^{-15}$ |
| (1,1) | 3143 | 0.0[c] | 0.0 | $0.86 \times 10^{6}$ | 0.66 | 0.0 |

[a] $\lambda_0$ is the wavelength of the band origin, $F_\lambda$ is the solar spectral flux, $G$ is the total solar induced excitation rate, $A$ is the spontaneous emission Einstein coefficient, $R$ is the branching ratio, and $\sigma$ is the absorption cross section. [b] Based on Doppler width of 0.016 $cm^{-1}$ (hwhm) at 30 K. [c] Only $v'' = 0$ is populated in the supersonic expansion.

Calculation of the detector signal is governed by two light transmission integrals through the exhaust gases: (1) the transmission of the local OH(A−X) emission from each point along the spectrograph line-of-sight (LOS) to the spectrograph, referred to as path $s$, and (2) the local excitation rate of OH(A) which depends on the transmission of the solar light to each point in the exhaust flow, referred to as path $s'$. For the formation of OH(A) via Ly-α photodissociation of $H_2O$, the detector signal intensity is given by

$$I = \chi_{H_2O}\epsilon F_{Ly\alpha}\sigma\int_0^\infty ds\ \rho(s)\exp(-\chi_{H_2O}\sigma\int_s^\infty ds'\ \rho'(s')) \quad (7)$$

where $\chi_{H_2O}$ is the mole fraction of water, $\epsilon$ is the conversion efficiency of absorbed Ly-α photons to OH(A), $F_{Ly\alpha}$ is the solar flux, and $\sigma$ is the absorption cross section. Because the OH(A) formed by Ly-α photodissociation is produced preferentially in very high rotational levels, there is very little absorption by the much colder exhaust OH(X); thus the transmission from each LOS point to the spectrograph is taken to be unity. The water mole fraction for the PRCS motor is taken to be $\chi_{H_2O} = 0.41$ (Table 1), which corresponds to the inner oxidizer-rich zone of the film-cooled motor.[30] This is appropriate since the detector LOS for the PRCS measurements falls within this zone. The conversion efficiency $\epsilon = 0.13$ is based on recent laboratory measurements;[26] however, it is noted that earlier measurements favor a somewhat lower value of 0.08.[44] The Ly-α solar flux of $F_{Ly\alpha} = 3.5 \times 10^{11}$ photons $s^{-1}$ $cm^{-2}$ is based on satellite data for the actual measurement time,[45] and the absorption cross section of $\sigma = 1.2 \times 10^{-17}$ $cm^2$ is based on laboratory data.[44]

Computation of the signal due to solar-induced fluorescence of the exhaust OH proceeds along similar lines, yielding

$$I_{v',v''} = \chi_{OH}R_{v',v''}G_{v',0}\int_0^\infty ds\ \rho(s) \times \exp(-\chi_{OH}\sigma_{v',0}\int_s^\infty ds'\ \rho(s'))\exp(-\chi_{OH}\sigma_{v',v''}\int_0^s ds''\ \rho(s'')) \quad (8)$$

where $I_{v',v''}$ is the emission intensity (photons $s^{-1}$ $cm^{-2}$) between the OH(A,$v'$) and OH(X,$v''$) vibrational levels, $\chi_{OH}$ is the OH exhaust mole fraction, $R_{v',v''}$ is the branching ratio, $G_{v',0}$ is the total solar-induced excitation rate into the OH(A,$v'$) manifold (only $v'' = 0$ is populated in OH(X) due to the supersonic expansion process), $\sigma_{v',v''}$ is an effective line absorption cross section averaged over the emission−absorption band rotational manifold, and the two exponential terms account for the transmission along the solar and emission paths, respectively. The determination of the $R$ and $G$ factors for solar-induced molecular fluorescence is straightforward[46,47] and depends only on the well-established Einstein $A$ and solar flux values for each band. The values used in this study are found in Table 4. The effective absorption cross section for each band was estimated based on the effective number of emission lines (there are approximately eight significant lines for each band at the retrieved OH(A) rotational temperature of 125 K) and a Doppler line width determined by a representative translational temperature for the vacuum expansion (the translational temperature was taken to be 30 K based on previous analysis of a similar motor).[48] Values for the cross sections are also given in Table 4.

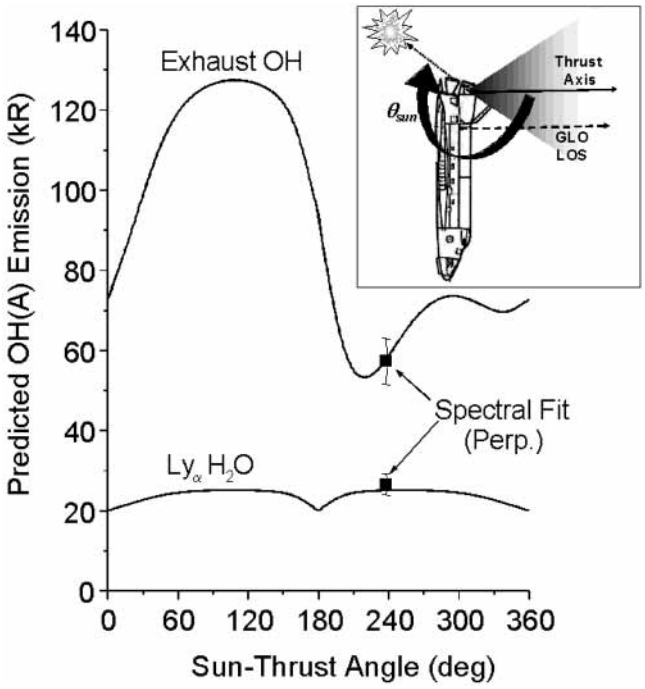


**Figure 6.** Predicted variation of the integrated intensities with the sun-thrust angle (see the insert for definition of the geometry) for the exhaust OH and Ly-α photoinduced components.

The mole fraction of OH in the exhaust is not well-determined. An initial estimate based on an earlier analysis used $\chi_{OH} = 4.4 \times 10^{-3}$ based on nozzle flow/chemical kinetic calculations for the inner oxidizer-rich zone of the PRCS.[30] The details of the flow and chemistry within a nozzle are extremely complex and not completely understood, hence the large uncertainty associated with the prediction of a trace species, such as OH. Consequently, the OH mole fraction was treated as an adjustable parameter, its value determined by fitting to the data. A value of $\chi_{OH} = 2 \times 10^{-3}$ was found to account for the solar-induced OH emission.

Figure 6 plots the predicted OH(A−X) emission intensities for the $H_2O$ and OH source components as a function of sun-thrust axis angle. The figure also includes an inset that defines the sun-thrust angle in the perpendicular day measurement. The sun-thrust axis angle governs the integration path through the exhaust cloud, and consequently determines the opacity of the experiment. The variation of the predicted signal is relatively mild for the photodissociation (Ly-α $H_2O$) component. In contrast, the resonance fluorescence OH component displays a much stronger variation with the sun-thrust axis angle. This is due to the much larger optical opacity for the component transitions.

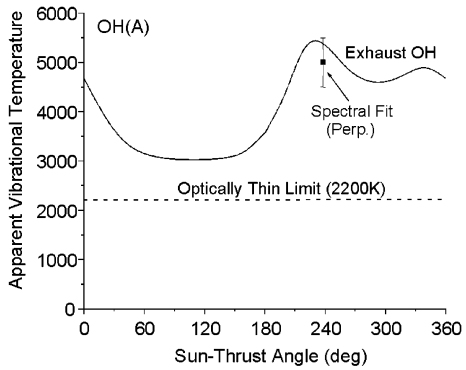


**Figure 7.** Predicted variation of the apparent vibrational temperature for the exhaust OH(A) fluorescence with the sun-thrust angle for the same geometry as in Figure 6.

The derived radiances from the perpendicular day spectrum are also shown in Figure 6 at the respective angle. The agreement between model and spectral analysis is considered acceptable given the approximate nature of the model, the uncertainties associated with the model parameters, and specification of the measurement geometry. The estimated uncertainty range for the model predictions is approximately ±25%.

An interesting consequence of the significant optical opacity is its effect on the apparent vibrational temperature for the exhaust OH(A) emission. Since the absorption cross section is much larger for the (0,0) band than the (1,0) and (1,1) bands, the effect of opacity is to increase the relative signal observed from the $v' = 1$ level. This translates into an increase in the apparent vibrational temperature for OH(A). The vibrational temperature is derived from the apparent ratio of vibrational populations for the $v' = 1$ and 0 levels. For the model calculations, the population ratio follows from

$$\frac{P_1}{P_0} = \frac{I_{1,0} + I_{1,1}}{I_{0,0}} \frac{A_{0,0}}{A_{1,0} + A_{1,1}} \tag{9}$$

where $P$ is the OH(A) population, $I$ is the computed intensity, and $A$ is the Einstein coefficient. The calculated temperatures are displayed in Figure 7. Good agreement is found with the 5000 K temperature estimate based on the spectral analysis.

## IV. Discussion

The present analysis of OH(A−X) emissions in the shuttle environment sheds new light on their sources. Daytime radiances can be accurately quantified with a model that includes resonance fluorescence excitation of trace amounts of cold OH present in the exhaust, process 4, and photodissociation of the primary exhaust constituent $H_2O$ through Ly-α and far-UV, process 3. The substantial photoinduced far UV contribution arises from the solar UV spectrum below Ly-α and is primarily due to a handful of atomic transitions, most notably OVI (1032−1036 Å) and CIII (977 Å).[49] These lines provide ∼2 eV more excess energy in process 3 than the 1.06 eV generated by Ly-α. The total UV flux at wavelengths below Ly-α is $\sim 2.6 \times 10^{11}$ photons $s^{-1}$ $cm^{-2}$,[49] somewhat smaller than the $3.5 \times 10^{11}$ photons $s^{-1}$ $cm^{-2}$ for Ly-α. However, the determined integrated intensity for the far-UV component is significantly larger than that for Ly-α, 40 vs 27 kR. Since the absorption cross sections for the far-UV lines are close to that for Ly-α,[44,50] this implies that the OH(A) conversion efficiency for the far-UV lines is $\epsilon = 0.26 \pm 0.13$, twice that for Ly-α.

The absolute radiances provide OH and $H_2O$ densities representative of the LOS−thrust axis intersection point that

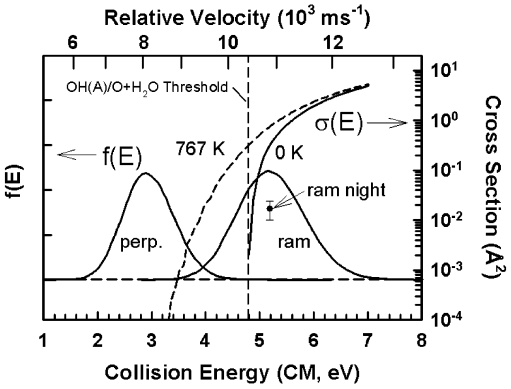


**Figure 8.** Collision energy distributions at perpendicular and ram geometries calculated for the ram night orbit condition. A $3.5 \times 10^3$ m $s^{-1}$ exhaust velocity is assumed. The cross section energy dependence given by eqs 11 and 12 for reaction 1 is also shown on a logarithmic scale for O atom translational temperatures of 0 and 767 K. The cross sections are compared to the value derived from the observed integrated OH(A−X) radiance during the ram night engine burn.

are within uncertainties consistent with predicted values.[30] As demonstrated nicely in Figures 6 and 7, an important characteristic of remote observation experiments is the viewing geometry, which has important effects on the degree of optical opacity, to the extent that apparent vibrational distributions depend on it. The day spectrum observed during a ram firing exhibits traces of signal in high $K$ regions of the spectrum that are not apparent in perpendicular observations. A comparable broad band is observed in the night ram spectrum. The night perpendicular spectrum is devoid of OH(A−X) radiance. The night ram emissions are, therefore, attributed to a translational energy enhanced collisional process between exhaust molecules and atmospheric constituents, the most abundant of which is atomic oxygen.

As stated in the Introduction, reaction 1 has been considered to be the main source of OH(A−X) emissions observed in the night spectra of exhaust afterglow. The energetics of this reaction system at the ram night conditions (Table 2) are depicted in Figure 8, where the center-of-mass (CM) collision energy distributions for the ram and perpendicular nominal relative velocities, $v_{rel}$, are shown. An $H_2O$ translational temperature of 30 K is assumed. The distributions are calculated using a Monte Carlo integration approach from the corresponding velocity shifted Maxwellian velocity distributions:

$$f(v)\,\mathrm{d}v = \left(\frac{m'}{2\pi kT'}\right)^{3/2}\left(\frac{m''}{2\pi kT''}\right)^{3/2} \exp\left(-\frac{m'(v_x'^2 + v_y'^2 + v_z'^2)}{2kT'}\right) \times \exp\left(-\frac{m''(v_x''^2 + v_y''^2 + v_z''^2)}{2kT''}\right) \mathrm{d}v_x'\,\mathrm{d}v_y'\,\mathrm{d}v_z'\,\mathrm{d}v_x''\mathrm{d}v_y''\mathrm{d}v_z'' \tag{10}$$

$$\mathbf{v} = \mathbf{v}_{rel} + \mathbf{v}' + \mathbf{v}''$$

where $\mathbf{v}'$ and $\mathbf{v}''$ are the thermal random velocity vectors of the oxygen atoms and the exhaust $H_2O$, respectively. The threshold of 4.79 eV is also identified in the figure. From the distributions it is determined that, at perpendicular conditions, essentially no reactants have collision energies above the OH(A) formation threshold, consistent with the fact that no OH(A−X) emissions could be identified. In the ram conditions, 76% of reactants are found to exceed that threshold.

Figure 8 also plots the previously estimated reaction cross section threshold function based on the Arrhenius expression

of eq 2.[16,21] The rate coefficient translates into the following cross section energy dependence given by a modified line-of-centers form:[51−53]

$$\sigma(E) = \sigma_0 \frac{(E - E_a)^n}{E}; \qquad E \geq E_a \tag{11}$$

$$\sigma_0 = 8.08\ \text{Å}^2\ \text{eV}^{-0.8}; \qquad n = 1.8$$

where $\sigma_0$ is a scaling parameter and $n$ determines the cross section growth curvature. The plot of eq 11 shown in Figure 8 (solid line) corresponds to the 0 K threshold function. The thermally broadened threshold function at the thermospheric temperature of 767 K (dashed line):

$$\sigma(E,T') = \langle \sigma(E) \rangle_{T'} \tag{12}$$

is also shown, demonstrating a substantial increase in effective cross section at nominal collision energies near threshold.

As mentioned in the Introduction, application of eq 2 or 11 results in an overprediction of the OH(A−X) emissions when incorporated in direct simulation Monte Carlo models of the spacecraft environment. The ram night viewing geometry allows a simple estimate of the cross section for reaction 1. Given the significant densities of the exhaust jet (eq 6), the oxygen atoms penetrating the exhaust suffer multiple collisions and do not reach the spacecraft. Consequently, since the spectrograph LOS is into the atmospheric wind, all of the incoming oxygen atoms undergo an energetic collision within the instrument field of view. The cross section can, therefore, be determined from

$$\sigma_{ram} = \sigma_{el}\epsilon_r = \sigma_{el}\frac{I}{[O]v_{rel}\chi_{H_2O}} \tag{13}$$

where $\sigma_{el}$ is the elastic cross section at the respective relative velocity, $\epsilon_r$ is the OH(A) conversion efficiency per O + $H_2O$ collision, $I$ is the integrated photon flux, and [O] is the atomic oxygen density. We have adopted an elastic cross section of 11 Å$^2$ for the respective relative velocity, using the criteria applied in the industry-standard direct simulation Monte Carlo program SOCRATES.[54] Applying the ram night conditions of Table 2 and the radiance shown in Table 3, a conversion efficiency of $1.5 \times 10^{-3}$ is determined corresponding to a chemiluminescence cross section associated with process 1 of $1.7 \times 10^{-2}$ Å$^2$. This value, depicted in Figure 8, is consistent with the analysis of Erofeev et al.,[22] who derived an estimated cross section of $10^{-2}$ Å$^2$ from the analysis of Soyuz engine activity as observed from Mir. It must be noted that the present estimated emission cross section should be regarded as an upper limit, because eq 13 assumes that all elastic collisions result in sufficient momentum transfer that subsequent collisions with $H_2O$ are below the OH(A) formation threshold. Momentum transfer, however, becomes less significant for elastic processes at high relative velocities. Currently, a unified approach does not exist for the derivation of a momentum transfer cross section for molecular systems at the hyperthermal velocities of interest in this work.[55] Fast oxygen atom beam angular scattering experiments, however, have provided interaction potentials associated with classical elastic scattering cross sections that are significantly lower than those currently applied in most models.[22,56]

With reference to Figure 8, it can be seen that eqs 11 and 12 predict a value of 1.7 Å$^2$ for process 1 at a relative velocity of $10.88 \times 10^3$ m s$^{-1}$, or a collision energy of 5.2 eV. This is 2 orders of magnitude above the present analysis. It is, therefore, not surprising that previous efforts to model OH(A−X) emissions based on the O + $H_2O$ reaction resulted in an overprediction of the emissions. These authors, however, did not take into account that sufficient energy is available to produce OH(A) in vibrational levels that predissociate, and, therefore, a significant fraction of OH(A) products do not radiate. If, in fact, the tentative assignment of $v' = 2$, 3, and 4 OH(A−X) emission bands in the night ram spectrum is correct (Figure 5), the fluorescence quantum yields[39,40,57−59] of the respective predissociated vibrational states dictate that the total cross section of reaction 1 could exceed 1 Å$^2$. Consequently, the reaction cross section given by the estimated rate constant may not be as poor as the initial comparison to the emission cross section may have suggested. On the other hand, a large cross section of the order of 1 Å$^2$ would not appear to be consistent with potential energy surface calculations by Matsika and Yarkony[24] that imply a constrained system governed by a collinear conical intersection through which the system must pass to access the surface associated with OH(A) + OH products. The bands attributed to $v' > 2$ predissociated states have also been observed in atmospheric pressure air plasmas by Levin and co-workers,[38] who attributed them to a reverse predissociation mechanism. We do not have a plausible explanation for this band at the current low-density conditions.

While the present analysis focuses on processes 1, 3, and 4, other possible sources of rotationally hot OH(A) could include the sequential processes

$$h\nu + H_2O \rightarrow 2OH(X) \tag{14a}$$

$$h\nu + OH(X) \rightarrow OH(A) \tag{14b}$$

$$O + H_2O \rightarrow 2OH(X) \tag{15a}$$

$$h\nu + OH(X) \rightarrow OH(A) \tag{15b}$$

where the second step involves photoexcitation of hot OH(X), and direct collisional excitation between exhaust species and atmospheric neutrals:

$$N_2, O + OH(X) \rightarrow N_2, O + OH(A) \tag{16}$$

made possible due to the high OH exhaust mole fraction. It is noted that, while there is a significant exhaust mole fraction of $H_2$ (∼0.04), the center-of-mass translational energy of reaction O + $H_2$ → OH(A) + H is well below threshold for the ram thrust geometry.

The significant difference in OH(A−X) intensity between the daytime ram−perpendicular difference spectrum and the ram night spectrum (Figure 2, Table 3) suggests additional daytime sources are contributing. Simple estimation establishes that the photoinduced sequential process (14) is at least several orders of magnitude below the daytime ram−perpendicular difference. However, we estimate that the collision-induced sequential process (15) can yield up to ∼100 kR at the daytime conditions. This estimate assumes a gas-kinetic reaction cross section of ∼10 Å$^2$ for the first O + $H_2O$ step. The literature rate coefficient for this reaction[19,20] is only valid for temperatures between 300 and 2500 K and results in cross sections at temperatures corresponding to ram relative velocities that are higher than what is physically possible. The magnitude of process 15 can be estimated directly from the data in Table 3 assuming that the day ram−perpendicular difference (44 kR) should be largely due to process 15 and reaction 1. If we assume that the perpendicular viewing geometry does not produce any radiance through this sequential mechanism, we can subtract off reaction 1 contributions by using the night ram data scaled for the

variation in the atmospheric O atom density for the day and night ram firings (31 kR). This yields 13 kR, implying that the cross section for the first step of process 15 is ~1 Å$^2$ at ram conditions. This is a lower limit since the assumption that no radiance is produced through this mechanism at perpendicular conditions signifies that the O atom flux is significantly attenuated by the exhaust jet, and the OH(X) products are swept out of the field of view prior to excitation and observation. Comparison of nighttime ram and perpendicular NH(A−X) emission intensities in the same experiment, however, indicate only a factor of ~2 attenuation of the perpendicular intensity. Based on an analysis of Space Shuttle as well as DSMC simulations,[13] the respective chemiluminescent reaction between atomic oxygen and a number of possible exhaust constituents is estimated to have a threshold of 2.5 eV. A detailed DSMC analysis of the present system is thus necessary to fully quantify the contribution of process 15 and the current daytime perpendicular measurements.

In case of collisional excitation events that yield OH(A) as shown in (16), there is virtually no information available in the literature on the O + OH forward reaction or the reverse quenching process. There are also other reaction pathways available at lower energies, namely production of H + $O_2$ (or $HO_2$, if collisionally stabilized) and O($^1$D) + OH(X), which can be expected to compete effectively with the nonadiabatic channel that would produce OH(A). From the known densities, a fluorescence excitation cross section of several square angstroms would be needed to account for the observed emission intensities. Future experimental and/or theoretical studies of this nonadiabatic process are, nevertheless, warranted. While the ram translational energy of an O + OH encounter is approximately 5.1 eV, the corresponding center-of-mass collision energy associated with an $N_2$ + OH collision is 6.5 eV, making this process competitive with the O + OH system.

Other potential sources of OH(A) considered include the well-known flame mechanisms[60]

$$OH + OH + H \rightarrow OH(A) + H_2O \quad (17)$$

$$O + H + M \rightarrow OH(A) + M \quad (18)$$

and optical excitation of the OH(X) in the engine exhaust flow by the OH(A) flame luminescence from the not directly viewed region in and around the engine. The former is ruled out because the exhaust flow density intercepted by the sensor line-of-sight is sufficiently low (the maximum viewed pressure is on the order of $10^{-5}$ atm for the PRCS engines), thereby rendering the three-body recombination flame mechanisms unimportant. The latter is ruled out because (1) no OH(A) emission is observed above the noise level for the night perpendicular PRCS burn, and (2) this mechanism would be exciting very rotationally cold OH(X) from the exhaust flow vacuum expansion and thus would produce a very narrow spectral emission distribution, whereas the night ram spectrum is quite rotationally hot.

While the single-step process of reaction 1 is currently the favored pathway for reactively producing OH(A), the possibility of two sequential chemical reactions initiated by the encounter of O and another exhaust plume species has yet to be fully explored. Recent, unpublished analysis by W. Dimpfl of the Aerospace Corporation[61] of satellite-based measurements of UV spectra and imagery of a Shuttle OMS engine ram burn at ~300 km altitudes indicate that a mechanism involving two chemical reaction steps may be an important source of OH(A).

Although the present work has focused on engine exhaust interactions with the atmosphere, the daytime signals and analysis suggest that OH(A−X) radiances can be exploited to diagnose contamination problems in space. A particularly difficult problem encountered on structures such as the International Space Station is the proper detection of leaks. The present measurements indicate that the origin of such leaks can be detected with an imager filtered at ~3090 Å and situated in a servicing vehicle to the station.

## V. Conclusions

OH(A→X) emission spectra observed in the Space Shuttle environment in regions of PRCS engine exhaust−atmosphere interactions have been analyzed at differing solar and jet direction configurations. The spectra were acquired along lines-of-sight parallel and close to the thrust axis for ram (directly into the atmospheric wind) and perpendicular firings for both daytime and nighttime solar illumination conditions, all at an altitude of ~390 km. Because of the good spectral resolution and multitude of observation conditions, it was possible to identify and quantify four separate OH(A) excitation mechanisms. These include (i) solar-induced fluorescence of the OH(X) in the PRCS exhaust flow, (ii) solar-induced photodissociation of $H_2O$ in the PRCS exhaust at the strong Lyman-α solar emission line (1216 Å), (iii) solar-induced photodissociation of $H_2O$ in the far UV, below Lyman-α, and (iv) collision processes between atmospheric and exhaust species, most probably the chemical reaction between the atmospheric atomic oxygen and exhaust $H_2O$. The daytime perpendicular spectrum can be modeled with components of mechanisms (i)−(iii) where only the OH(A) state distributions from far-UV photodissociation require adjustments of vibrational and rotational distribution. The OH(A) state distributions of mechanisms (i) and (ii) are given by the OH(X) rotational temperature in the expansion-cooled exhaust and excitation Franck−Condon factors, and laboratory measurements, respectively. The analysis permitted the derivation of a far-UV $H_2O$ to OH(A) conversion efficiency of 0.26 ± 0.13. Calculated integrated radiances produced through $H_2O$ photodissociation are in excellent agreement with the observed intensities, assuming the modeled $H_2O$ exhaust mole fraction of 0.41.[30] The calculated radiance associated with mechanism (i) is in agreement with the observed intensities if an OH mole fraction of 0.002 in the exhaust is assumed.

The nighttime ram spectrum is most probably attributed to reaction 1 and is associated with high rotational excitation ($T_r'$ = 4000 K) and very high vibrational excitation. No OH(A−X) emissions could be identified during perpendicular night engine operation. This is consistent with the fact that collisions with translational energies surpassing the 4.79 eV threshold of reaction 1 are not possible at the perpendicular condition, while ~76% of reactant collisions are determined to have energies exceeding threshold for the ram conditions. The integrated OH(A−X) intensities in the ram night measurement are associated with a chemiluminescence cross section of $1.7 \times 10^{-2}$ Å$^2$. This value depends on knowledge of the appropriate momentum transfer cross section, but is significantly lower than cross sections applied in previous modeling efforts of OH(A−X) emissions in the spacecraft environment. The spectrum exhibits evidence for bands associated with predissociated states, implying that significant amounts of OH(A) products are formed that do not radiate, and that the total OH(A) formation cross section could be several orders of magnitude higher, which could be in conflict with the constrained dynamics expected from the reported conical intersection mechanism.[24] More detailed studies of the dynamics of reaction 1 as well as alternative processes 14−16 are warranted.

**Acknowledgment.** We thank George Karabadzhak, Jim Duff, Matt Braunstein, and Frank Marcos for many helpful and insightful discussions. The authors express their appreciation to Bill Dimpfl for sharing the results of his preliminary analysis of the Shuttle OMS burns. The authors gratefully acknowledge support from the Air Force Office of Scientific Research under Task 2303ES02 and Contract No. F49620-01-1-0095 (Program Manager: Michael R. Berman) and Task 2301HS (Program Manager: Kent Miller). We also acknowledge support from AFOSR with Mitat Birkan as the technical monitor.

## References and Notes

(1) Black, J. H.; Dalgarno, A. *Astrophys. Lett.* **1973**, *15*, 79.
(2) Herbst, E.; Schubert, J. G.; Certain, P. R. *Ap. J.* **1977**, *213*, 696.
(3) Gerlich, D. *Adv. Chem. Phys.* **1992**, *82*, 1.
(4) Viereck, R. A.; Murad, E.; Green, B. D.; Joshi, P.; Harbaugh, G.; Hieb, R. *Nature* **1991**, *354*, 48.
(5) Broadfoot, A. L.; Anderson, E.; Sherard, P.; Knecht, D. J.; Viereck, R. A.; Pike, C. P.; Murad, E.; Elgin, J. E.; Bernstein, L. S.; Kofsky, I. L.; Rall, D. L. A.; Blaha, J.; Culbertson, F. L. *J. Geophys. Res.* **1992**, *97*, 19501.
(6) *Contamination glow observed during two rocket sounding experiments*; Clemesha, B. R., Takahashi, H., Sahai, Y., Eds.; Kluwer: Dordrecht, 1988.
(7) Zhou, D. K.; Pendleton, J.; W. R.; Bingham, G. E.; Thompson, D. C.; Raitt, W. J.; Nadile, R. M. *J. Geophys. Res.* **1994**, *99*, 19.
(8) Boraas, S. *J. Spacecraft Rockets* **1987**, *24*, 539.
(9) Clifton, K. S.; Owens, J. K. *Appl. Opt.* **1987**, *27*, 603.
(10) Trinks, H.; Hoffman, R. J. In *Spacecraft Contamination: Sources and Prevention*; Roux, J. A., McCay, T. D., Eds.; American Institute Aeronautics Astronautics: New York, 1984; Vol. 91, p 261.
(11) Broadfoot, A. L. http://glo.lpl.arizona.edu/glo.
(12) Broadfoot, A. L.; Sandel, B. R.; Knecht, D. J.; Viereck, R. A.; Murad, E.; *Appl. Opt.* **1992**, *31*, 3083.
(13) Viereck, R. A.; Murad, E.; Knecht, D. J.; Pike, C. P.; Bernstein, L. S.; Elgin, J. B.; Broadfoot, A. L. *J. Geophys. Res.* **1996**, *101*, 5371.
(14) Karabadzhak, G. F.; Pastinin, Y.; Khmelinin, B.; Teslenko, V.; Shvets, N.; Drakes, J. A.; Swann, D. A.; McGregor, W. K. In *36th AIAA Aerospace Sciences Meeting & Exhibit*, Reno, NV, 1998; Vol. AIAA 98-0288.
(15) Karabadzhak, G. F.; Pastinin, Y.; Afanasiev, A.; Szhenov, E.; Drakes, J. A.; McGregor, W. K.; Bradley, D.; Teslenko, V.; Shvets, N.; Volkov, O.; Kukushkin, V. In *37th AIAA Aerospace Sciences Meeting & Exhibit*, Reno, NV, 1999; Vol. AIAA 99-1042.
(16) Drakes, J. A.; Sann, D. G.; Karabadzhak, G. F.; Plastinin, Y. In *37th AIAA Aerospace Sciences Meeting & Exhibit*, Reno, NV, 1999; Vol. AIAA 99-0975.
(17) Gimelshein, S. F.; Levin, D. A.; Drakes, J. A.; Karabadzhak, G. F.; Ivanov, M. S. In *33rd Thermophysics Conference*, Norfolk, VA, 1999; Vol. AIAA 99-3452.
(18) Gimelshein, S. F.; Levin, D. A.; Drakes, J. A.; Karabadzhak, G. F.; Plastinin, Y. *J. Thermophys. Heat Transfer* **2002**, *16*, 58.
(19) Tsang, W.; Hampson, R. F. *J. Phys. Chem. Ref. Data* **1986**, *15*, 1087.
(20) Cohen, N.; Westberg, K. R. *J. Phys. Chem. Ref. Data* **1983**, *12*, 531.
(21) Karabadzhak, G. F.; Pastinin, Y.; Szhenov, E.; Afanasiev, A.; Drakes, J. A.; McGregor, W. K.; Bradley, D.; Teslenko, V.; Shvets, N.; Volkov, O.; Kukushkin, V.; Gimelshein, S.; Levin, D. A. In *38th AIAA Aerospace Sciences Meeting & Exhibit*, Reno, NV, 2000; Vol. AIAA 2000-0105.
(22) Erofeev, A.; Friedlander, O.; Karabadzhak, G. F.; Plastinin, Y. In *22nd Symposioum on Rarefied Gas Dynamics*, Sydney, 2000.
(23) Orient, O. J.; Chutjian, A.; Murad, E. *Phys. Rev. A* **1990**, *41*, 4106.
(24) Matsika, S.; Yarkony, D. R. *J. Chem. Phys.* **2002**, *117*, 3733.
(25) Mordaunt, D. H.; Ashfold, M. N. R.; Dixon, R. N. *J. Chem. Phys.* **1994**, *199*, 7360.
(26) Harich, S. A.; Hwang, H. D. W.; Yang, X.; Lin, J. J.; Yang, X.; Dixon, R. N. *J. Chem. Phys.* **2000**, *113*, 10073.
(27) Carrington, T. *J. Chem. Phys.* **1964**, *41*, 2012.
(28) Pickett, J. S.; Murphy, G. R.; Kurth, W. S.; Goertz, C. K.; Shawhan, S. D. *J. Geophys. Res.* **1985**, *90*, 3487.
(29) Pickett, J. S.; Murphy, G. B.; Kurth, W. S. *J. Spacecraft Rockets* **1988**, *25*, 169.
(30) Viereck, R. A.; Bernstein, L. S.; Mende, L. S.; Murad, S. B.; Swenson, E. *J. Spacecraft Rockets* **1993**, *30*, 724.
(31) Hedin, A. E. The NRL Mass Spectrometer, Incoherent Scatter Radar Extended Model: NRLMSISE-00; http://uap-www.nrl.navy.mil/models_web/msis/msis_home.htm.
(32) Hedin, A. E. *J. Geophys. Res.* **1991**, *96*, 1159.
(33) Hedin, A. E. *J. Geophys. Res.* **1987**, *92*, 4649.
(34) Rishbeth, H. *J. Atmos. Solar-Terrestrial Phys.* **2002**, *64*, 1351.
(35) Narcisi, R. S.; Trzcinski, E.; Federico, G.; Wlodyka, L.; Delorey, D. In *AIAA Conference on the Space Shuttle*; AIAA: Washington, DC, 1983; Vol. AIAA 83-2659.
(36) Knecht, D. J.; Murad, E.; Viereck, R.; Pike, C. P.; Broadfoot, A. L.; Anderson, E. R.; Hatfield, D. B.; Stone, T. C.; Sandel, B. R. *Adv. Space Res.* **1997**, *19*, 627.
(37) Berk, A.; Bernstein, L. S.; Richtsmeier, S. C.; Cox, J. W.; Slack, M. W. In *1990 Meeting of the IRIS Specialty Group on Targets, Backgrounds, and Discrimination*; 1990; Vol. 1, p 69.
(38) Levin, D. A.; Laux, C. O.; Kruger, C. H. *J. Quant. Spectrosc. Radiat. Transfer* **1999**, *61*, 377.
(39) Luque, J.; Crosley, D. R. *LIFBASE: Database and Spectral Simulation Program*, Version 1.5; SRI International, 1999.
(40) Yarkony, D. R. *J. Chem. Phys.* **1992**, *97*, 1838.
(41) Parlant, G.; Yarkony, D. R. *J. Chem. Phys.* **1999**, *110*, 363.
(42) Copeland, R. A.; Jeffries, J. B.; Crosley, D. R. *J. Mol. Spectrosc.* **1990**, *143*, 183.
(43) Brook, J. W. *J. Spacecraft Rockets* **1969**, *6*, 626.
(44) Lee, L. C. *J. Chem. Phys.* **1980**, *72*, 4334.
(45) Tobiska, W. K.; Pryor, W. R.; Ajello, J. M. *Geophys. Res. Lett.* **1997**, *24*, 1.
(46) Kassal, T. *Appl. Opt.* **1975**, *14*, 1513.
(47) Cageao, R. P.; Ha, Y. L.; Hang, Y.; Morgan, M. F.; Yung, Y. L.; Sander, S. P. *J. Quant. Spectrosc. Radiat. Transfer* **1997**, *57*, 703.
(48) Duff, J. W.; Bernstein, L. S. *J. Quant. Spectrosc. Radiat. Transfer* **1981**, *26*, 85.
(49) Curdt, W.; Feldman, U.; Laming, J. M.; Wilhelm, K.; Schule; Lemaire, P. *Astron. Astrophys. Suppl. Ser.* **1997**, *126*, 281.
(50) Watanabe, K.; Jursa, A. S. *J. Chem. Phys.* **1964**, *41*, 1650.
(51) Levine, R. D.; Bernstein, R. B. *J. Chem. Phys.* **1972**, *56*, 2281.
(52) Chesnavich, W. J.; Bowers, M. T. *J. Phys. Chem.* **1979**, *83*.
(53) Armentrout, P. B. *Int. J. Mass Spectrosc.* **2000**, *200*, 219.
(54) Cho, J.; Braunstein, M.; Elgin, J. B. *SOCRATES 3.0 User's Manual*; 1995.
(55) Wysong, I. J.; Dressler, R. A.; Chiu, Y.; Boyd, I. D. *J. Thermophys. Heat Transfer* **2002**, *16*, 83.
(56) Karabadzhak, G. Private communication.
(57) German, K. R. *J. Chem. Phys.* **1975**, *63*, 5252.
(58) Brzozowski, J.; Erman, P.; Lyra, M. *Phys. Scr.* **1978**, *17*, 507.
(59) Spaanjars, J. J. L.; Meulen, J. J. T.; Meijer, G. *J. Chem. Phys.* **1997**, *107*, 2242.
(60) Davis, M. G.; McGregor, W. K.; Mason, A. A. *J. Chem. Phys.* **1974**, *61*, 1352.
(61) Dimpfl, W. Private communication.
(62) Hedin, A. E. *J. Geophys. Res.* **1983**, *88*, 10170.